Large eddy simulations of the all-speed turbulent jet flow using 3-D CFD code GASFLOW-MPI

Han Zhang, Yabing Li*, Jianjun Xiao, Thomas Jordan

Institute of Nuclear and Energy Technologies, Karlsruhe Institute of Technology, Karlsruhe 76021, Germany

ARTICLE INFO

ABSTRACT

Turbulent flow at a wide range of Mach numbers may occur during design based accidents (DBA) or severe accidents in nuclear power plants (NPPs), for instinct, incompressible gas mixing flow (subsonic), gas mixture critical flow (transonic) or detonation (supersonic). All of them need to be simulated in safety analysis of NPP containments, therefore we need the computer code to have the capability to simulate all-speed flow. GASFLOW-MPI is a well-developed parallel all-speed CFD software used to predict gas turbulent mixing, chemical combustion and other related thermal-hydraulic phenomena in containments of NPPs. In order to validate the all-speed turbulent flow capability of GASFLOW-MPI, four turbulent jet cases over a broad range of Mach number have been performed in this paper. The large eddy simulation (LES) turbulent model is employed to capture more details of turbulence and flow features in this study. The standard Smagorinsky sub-grid scale model is utilized to model the unresolved turbulent behaviors at sub-grid scale. Both the instantaneous and time-averaged flow fields are analyzed as well as turbulent statistics to compare with the experimental data sets. The simulation results are in good agreement with the experimental data sets available in the literature. The shear layer instability is observed in the instantaneous flow field which leads to the end of the potential core and then the centerline velocity begins to decay. The size of the potential core and the decay rate of the centerline velocity are consistent well with the experiments. The turbulence intensity in the fully developed region agree well with the experimental data and the velocity power spectrum reveals the -5/3 law. Simulation results show that the compressibility has a significant effect on a free shear layer growing rate which is consistent with the experiments. The complex shock wave structure is also captured exactly by the second-order total variation diminishing (TVD) scheme. GASFLOW-MPI code has been successfully validated using the experimental data of turbulent jet flow at the wide regime of Mach numbers.

1. Introduction

Hydrogen will be generated during the severe accidents in nuclear power plants (NPPs) mainly due to cladding coolant interaction (Breitung, 1999), then it may be injected into containment from the break in the first loop. Flammable clouds may be formed inside the containment which could pose a great threat to the integrity of the containment. In the Fukushima accident, hydrogen explosions inside the reactor buildings in units 1, 3 and 4 of Fukushima Daiichi NPPs damaged structures and caused the release of large amounts of radioactive material into the atmosphere (IAEA, 2011). Due to the broad variety of accident scenarios in NPPs, gas turbulent flow at different Mach number, existing in containment during both Design Based Accidents (DBA) and severe accidents, have significant influence for containment thermal hydraulics. Firstly, the main transportation of gas mixture in containment is in the domain of incompressible turbulent

flow (Sarikurt and Hassan, 2017) ($Ma < 0.3$) (Ferziger and Peric, 1996). Meanwhile, according to the report of Containment Code Validation Matrix (Chin et al., 2014), the gas mixture critical flow ($Ma = 1$) that may happen at the break, valves, orifices or other obstructions to the flow ranks major for both DBA and severe accident in the Containment Thermal-hydraulics Phenomena Identification Ranking Table (PIRT) for NPPs (Chin et al., 2014). Hydrogen flame acceleration ($Ma < 1$) and detonation ($Ma > 1$) also ranks major among Containment Thermal-hydraulics PIRT (Chin et al., 2014). To sum above, for containment thermal-hydraulics simulation, turbulent flow at the broad regime of Mach numbers should be simulated, from subsonic (incompressible flow) to transonic (critical flow), even supersonic (detonation). Therefore, a solution algorithm valid for all-speed flow is needed.

The hydrogen risk analysis CFD code TONUS-CFD employs two solvers (Kudriakov, 2008), in order to simulate the flow at a wide range of Mach numbers in NPPs. One is the pressure-based implicit method

---
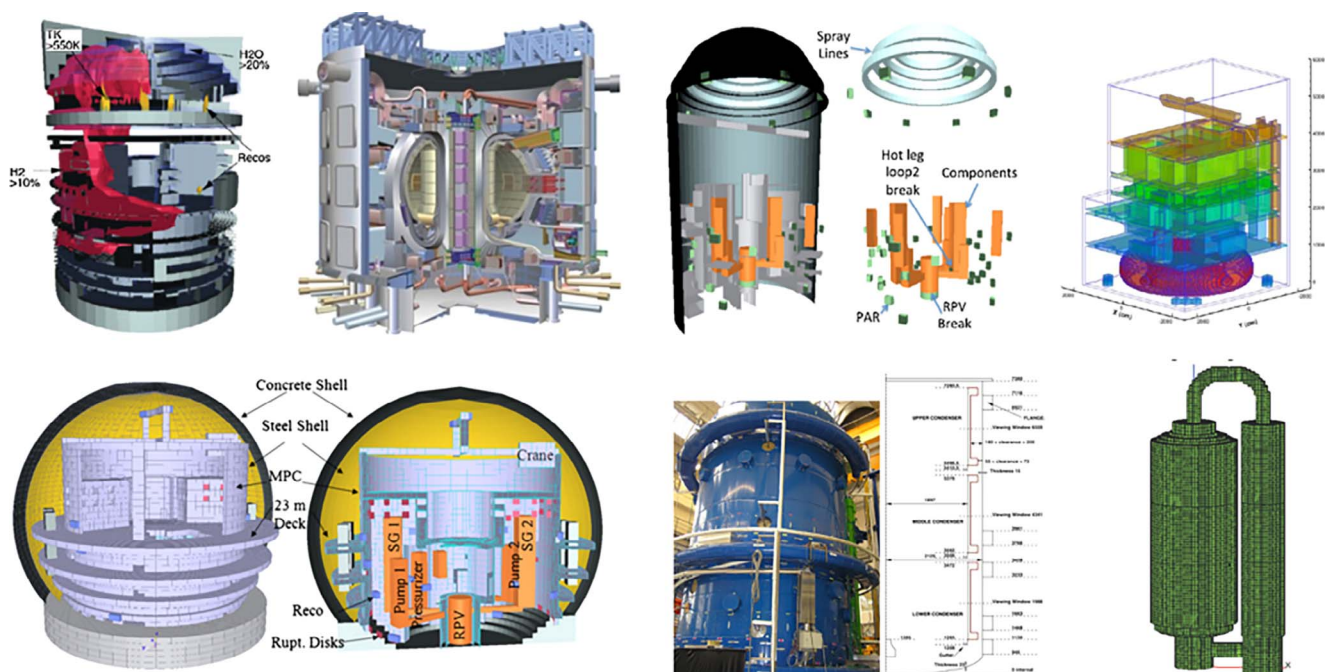
Fig. 1. NPPs containment applications and international benchmarks.

for low Mach number flow and the other is the density-based explicit method for high Mach number flow. A similar strategy is employed in the commercial CFD code Fluent (Fluent, 2011). Different from the above CFD codes, GASFLOW-MPI is an all-speed flow CFD software using a unified numerical algorithm in one CFD code. Only one powerful all-speed flow semi-implicit pressure-based algorithm "ICE'd ALE" (Hirt, et al., 1974) is employed in GASFLOW-MPI to solve the wide range Mach number flow. In ICE'd ALE algorithm, the pressure equation is derived from the discrete continuity equation and momentum equation rather than from the continuous equations, which ensures the correct pressure field distribution could be obtained at the incompressible limit flow (Xiao et al., 2014a, b). Furthermore, the pressure equation is solved implicitly, which avoids the limitation of acoustic waves and allows bigger time step. The ICE'd ALE algorithm in GASFLOW-MPI has been widely validated by the single and integration cases, such as the lid-driven cavity flow and THAI benchmarks (Xiao et al., 2017; Royl et al., 2016). In order to capture the shock wave at the high Mach number flow, the well-known second-order accuracy total variation diminishing (TVD) scheme, van Leer MUSCL scheme with flux limiter (Van Leer, 1979), is performed. The validation of the van Leer MUSCL scheme in GASFLOW-MPI also has been made, such as the shock tube case and supersonic flow over forward facing step (Xiao et al., 2016, Xiao et al., 2017). The detailed validation matrices of GASFLOW are summarized in the GASFLOW validation manual (Royl et al., 2014).

It is well known that turbulence modeling is one of the key issues for successful simulation of all-speed turbulent flow. RANS model is a successful and widely used turbulent model. A two-equation RANS model, the standard $k-\varepsilon$ turbulent model, is used in GASFLOW-MPI and has been applied in many simulations successfully. However, it has been found that it always overpredicts the turbulent kinetic energy growth rate in high Mach number flow (Kaushik et al., 2015). Although several attempts have been made to improve the RANS performance for compressible flow (Zeman, 1990; Heinz, 2003), there are still several inherent shortcomings (Kaushik et al., 2015). Another disadvantage is that only averaged physical quantities could be resolved in RANS model and all turbulent fluctuation signals cannot be captured (Garnier et al., 2009). Large eddy simulation (LES) will help to understand flow physics better than RANS with the help of resolved detailed information.

Sarikurt claimed that for a situation like hydrogen buoyancy jet, or establish or erosion of stratification, or even further, an interaction between the jet and stratified layer, there was strong anisotropy and fluctuations due to buoyancy effect, which would not be captured in the two equation RANS models (Sarikurt and Hassan, 2017). Therefore, the LES turbulent model is employed in this paper to simulate the all-speed turbulent flow. LES model is a recently developed turbulent model in GASFLOW-MPI and the preliminary validation of LES model has been made by a low Mach number backward-facing step flow case (Zhang et al., 2017). The turbulent jet flow at different Mach number, which is a fundamental flow phenomenon in safety analysis of NPPs containment, is chosen to validate the all-speed CFD code GASFLOW-MPI.

This paper is organized as following. The conservation equations and the LES turbulent model in GASFLOW-MPI are introduced in Section 2. The solution algorithm of the all-speed solver "ICE'd ALE" is presented in Section 3. The numerical results are presented and discussed in Section 4. The conclusions are presented in Section 5.

2. Physical model

2.1. Conservation equation

GASFLOW-MPI is a well-developed parallel scalable CFD software (Xiao et al., 2014a,b) and has been utilized to predict the complex physical phenomena in NPP containments and other industrial facilities. GASFLOW has been well validated with the blind-/open-international benchmarks in the past decades, and been widely used to analyze the hydrogen risk and mitigation method in various types of nuclear containments (Royl, et al., 1995; Benz et al., 2013; Dimmelmeier et al., 2012; Kim and Hong, 2015; Li et al., 2018) as shown in Fig. 1. Many application physical models, including fluid dynamics module, turbulence module, phase change/heat transfer model, chemical reaction module and so on, are employed in GASFLOW-MPI to calculate the time-dependent composition distribution, temperature distribution, velocity distribution and pressure distribution in 3-D geometry. Since that only single phase, single component turbulent flow is simulated in this paper, the fluid dynamics module and turbulence module are employed. But heat transfer, phase change and chemical reactions are not considered. Therefore, the governing equation could be simplified as

following for convenience (Xiao et al., 2014a,b, 2017; b).

Volume equation

$$\frac{\partial V}{\partial t} = V\nabla\cdot(\mathbf{b}-\mathbf{u})$$

(1)

where $\mathbf{u}$ is the fluid velocity vector, V is the discretized fluid control volume and $\mathbf{b}$ is the control volume velocity surface vector incorporated in the simplified ALE methodology used in GASFLOW-MPI. When $\mathbf{b} = 0$ the equations are in Eulerian coordinates, and when $\mathbf{b} = \mathbf{u}$ the equations are in Lagrangian coordinates.

Mass equation

$$\frac{\partial \rho}{\partial t} = \nabla\cdot[\rho(\mathbf{b}-\mathbf{u})]$$

(2)

where ρ is the fluid density.

Momentum equations

$$\frac{\partial (\rho\mathbf{u})}{\partial t} = \nabla\cdot[\rho\mathbf{u}(\mathbf{b}-\mathbf{u})]-\nabla p + \nabla\cdot\boldsymbol{\sigma} + \rho\mathbf{g}-\nabla\cdot\widetilde{\boldsymbol{\sigma}}$$

(3)

where p, $\boldsymbol{\sigma}$ and $\mathbf{g}$ are the fluid pressure, viscous stress tensor and gravity acceleration, respectively, and $\widetilde{\boldsymbol{\sigma}}$ is the sub-grid scale (SGS) Reynolds stresses term. In GASFLOW-MPI, the Newton's law is used for the viscous stress tensor $\boldsymbol{\sigma}$ in momentum equation Eq. (3).

Internal energy equation

$$\frac{\partial (\rho I)}{\partial t} = \nabla\cdot[\rho I(\mathbf{b}-\mathbf{u})]-p\nabla\cdot\mathbf{u}-\nabla\cdot\mathbf{q}-\nabla\cdot\widetilde{\mathbf{q}}$$

(4)

where I is the fluid internal energy, is the energy flux vector and $\widetilde{\mathbf{q}}$ is the SGS heat flux term. The term $\widetilde{\mathbf{q}}$ is the second term. Both $\widetilde{\boldsymbol{\sigma}}$ and $\widetilde{\mathbf{q}}$ are modeled by the LES turbulent model which would be introduced in the next section. The Fourier's law is used for the energy flux vector in energy equation Eq. (4).

2.2. LES turbulent model

The large eddy simulation turbulent model is employed in the advanced parallel CFD code GASFLOW-MPI. A wide range of scale turbulent energy is resolved directly in LES method, and only the turbulence fluctuation at sub-grid scale should be modeled by SGS model, while in RANS model all the turbulent kinetic energy is modeled by the turbulent kinetic energy equation. Therefore compared with RANS model, the LES turbulent model is less sensitive to modeling errors (Salmanzadeh et al., 2010).

2.2.1. SGS Reynolds stresses term

The SGS Reynolds stresses $\widetilde{\sigma}$ in Eq. (3), resulting from filtering operations require modeling by LES SGS model since they are unknown, where the Boussinesq hypothesis is employed as following.

$$\widetilde{\sigma}_{ij} = -\mu_t\left(2S_{ij}-\frac{2}{3}S_{kk}\delta_{ij}\right)$$

(5)

where the rate-of-strain tensor $S_{ij} = (\partial u_i/\partial x_j + \partial u_j/\partial x_i)/2$ and μ_t is the SGS turbulent viscosity.

The Smagorinsky model is employed in GASFLOW-MPI to calculate the SGS turbulent viscosity due to its simplicity and practicality. The turbulent viscosity in the Smagorinsky model, is proposed by assuming that the turbulent energy transfers from the large resolved scales to the small sub-grid scales and the turbulent energy dissipation by the small sub-grid scales are in equilibrium (Smagorinsky, 1963; Piomelli, 1999). And the turbulent viscosity could be expressed by Eq. (6):

$$\mu_t = \rho L_s^2|S|$$

(6)

$$L_s = C_s\Delta$$

(7)

$$\Delta = V^{1/3} = (\Delta x\Delta y\Delta z)^{1/3}$$

(8)

$$|S| = \sqrt{2S_{ij}S_{ij}}$$

(9)

where L_s is the sub-grid scales mixing length and $|S|$ is an inner product of strain rate tensor, C_s is a constant in Smagorinsky model and Δ is the LES filter width. Different from the RANS model, the turbulent viscosity is a function of the mesh size in LES model. The value of the Smagorinsky constant C_s depends on the type of flow (Hassan, 2008). For the application, the Smagorinsky constant C_s is set to 0.1 based on former research to yield the best results (Fluent, 2011). The filter width Δ is computed from the geometry size of the computational cell as given in Eq. (8).

In implementation, the effects of the SGS Reynolds stress are considered by utilizing the effective viscous stress tensor $\sigma eff,ij$ as shown in Eq. (10).

$$\sigma_{eff,ij} = \sigma_{ij}-\widetilde{\sigma}_{ij} = \mu_{eff}\left(2S_{ij}-\frac{2}{3}S_{kk}\delta_{ij}\right) = (\mu + \mu_t)\left(2S_{ij}-\frac{2}{3}S_{kk}\delta_{ij}\right)$$

(10)

where μeff is the effective viscosity coefficient.

2.2.2. SGS heat flux term

The SGS heat flux term $\widetilde{\mathbf{q}}$ in the Eq. (4) is another unclosed term, and requires approximation within the SGS model. The sub-grid heat flux term is modeled using the gradient hypothesis and calculated by employing a turbulent Prandtl number Pr_t as Eq. (11) and (12) (Grotzbach and Worner, 1999). It should be noted that there are also more complicated SGS heat flux models, such as the first-order and second-order SGS models. The comparisons of different heat flux SGS models have been made, the results show that their results agree quite well (Nieuwstadt et al., 1993). Therefore, the SGS heat flux model, Eq. (11) and (12), is suitable for our applications.

$$\widetilde{q_j} = -\lambda_t\frac{\partial T}{\partial x_j}$$

(11)

$$\lambda_t = \frac{\rho\mu_t}{Pr_t}$$

(12)

where λ_t is the turbulent conductivity coefficient and Pr_t is the turbulent Prandtl number. The size of turbulent Prandtl number indicates the competition between energy turbulent fluctuation and the momentum turbulent fluctuation. A small value Pr_t means that at sub-grid scale the temperature fluctuation is much more intensive than that of velocity. In this paper, the turbulent Prandtl number Pr_t equals to 0.85.

In implementation, the effective heat flux is utilized to consider the turbulent effects as following.

$$q_{eff,j} = q_j + \widetilde{q_j} = -\lambda_{eff}\frac{\partial T}{\partial x_j} = -(\lambda + \lambda_t)\frac{\partial T}{\partial x_j}$$

(13)

Where λ_{eff} is the effective conductivity coefficient.

3. Numerical method

Generally speaking, the flow could be divided into the incompressible flow and compressible flow according to the Mach number. And most of CFD solvers are designed for either compressible flow ($Ma > 0.3$), such as the explicit density-based algorithms (Balzek, 2001), or incompressible flow ($Ma < 0.3$), such as the implicit pressure-based algorithms (Patankar and Spalding, 1972). However, it is a wide range of Mach number flow for a complete accident analysis in NPPs containment, which is a great challenge in numerical simulation. For instance, it could be a compressible jet flow near the nozzle and an incompressible plume flow far from the nozzle. If the flammable clouds are ignited in the containment, the deflagration and/or detonation may occur, which are both compressible reactive flow. The all-speed flow algorithm, Implicit Continuous Eulerian-Arbitrary Lagrangian-Eulerian (ICE'd ALE) method, is employed to cover all the physical phenomena of flammable clouds in the nuclear containment in the GASFLOW-MPI.

3.1. ICE'd ALE method

There are several numerical difficulties to achieve all-speed flow simulation. On one hand, it has been demonstrated in Refs. (Lee, 1991, Lee, 1996) that traditional schemes designed for compressible flow introduce an amount of artificial dissipation which does not scale correctly for incompressible limit flow. Therefore, the accuracy of such spatial discretization suffers for the low Mach number flow (Sesterhenn et al., 1999). On the other hand, the shock waves are one of the most fundamental phenomena in supersonic or transonic flow. It is characterized by an abrupt discontinuous change in physical quantities, such as pressure, temperature and density. Tracking shock, peculiarly when and where new shock arises, is extremely important in scientific and engineering applications but numerically troublesome (Chen, 2001). The ICE'd ALE method in GASFLOW-MPI has been carefully designed to overcome the above difficulties. And its features could be summarized as following.

1) ICE'd ALE method is a kind of pressure-based method. The pressure equation is derived from the discrete continuity equation and momentum equation rather than from the continuous continuity equation and momentum equation, which ensures accuracy of the spatial discretization for low Mach number flow.
2) The pressure variable is treated as the implicit scheme in ICE'd ALE method, which allows the time step to avoid the limitation of acoustic waves. The large time step ensures the computational efficiency of GASFLOW-MPI.
3) Different from the blended scheme in the original pressure-based all-speed flow algorithms (Karki and Patankar, 1989, Demirdžić, et al., 1993), an advanced second-order accuracy TVD scheme, van Leer MUSCL scheme, is utilized in GASFLOW-MPI to capture the shock wave accurately.
4) ICE'd ALE method employs the operator-splitting technology to avoid the iteration among velocity-pressure-energy. Compared with the SIMPLE-type all-speed flow algorithms, where an iteration exists among different physical fields, the computational performance of ICE'd ALE is much more efficient.

The calculation process of Navier-Stokes equation in ICE'd ALE method is divided into 3 phases by operator-splitting technique, which is second-order accuracy in the spatial term and first-order accuracy in the temporal term. The staggered grid mesh is used where scalar variables, such as pressure, temperature, are arranged at the cell centers, while the vector unknowns, such as the fluid velocities, are arranged at the cell edges. In ICE'd ALE method, the pressure, velocity and temperature are solved from the Navier-Stokes equation directly. In other words, these three variables are the unknowns in the Navier-Stokes equation system. The density is derived from the perfect gas law. The outline of the ICE'd ALE method is described as following (Xiao et al., 2014a, b).

At the first phase, a Lagrangian calculation is performed where the diffusion terms and source terms are calculated in explicit scheme.

$$\frac{V^A - V^n}{\Delta t} = \sum_f (\mathbf{u} \cdot \mathbf{A})^n_f \Delta S_f \tag{14}$$

$$\frac{(\rho V)^A - (\rho V)^n}{\Delta t} = 0 \tag{15}$$

$$\frac{(\rho V \mathbf{u})^A - (\rho V \mathbf{u})^n}{\Delta t} = -\sum_f [(p\mathbf{A})^n_f + (\sigma_{\mathbf{eff}} \mathbf{A})^n_f] \Delta S_f + \rho \mathbf{g} V^n \tag{16}$$

$$\frac{(\rho V I)^A - (\rho V I)^n}{\Delta t} = -p^n \sum_f (\mathbf{u} \cdot \mathbf{A})^n_f \Delta S_f - \sum_f (\mathbf{q_{eff}} \cdot \mathbf{A})^n_f \Delta S_f \tag{17}$$

$$p^A = \rho^A \frac{R}{M} T^A \tag{18}$$

where $\mathbf{A}$ is the outward normal vector and ΔS_f is the face surface.

At the second phase, a Lagrangian calculation is carried out where pressure waves are propagated in implicit scheme. In order to express the derivation of the elliptic pressure equation conveniently, a semi-discrete form is used here where only temporal term is discretized. And the second-order central difference is employed to discrete the elliptic pressure equation Eq. (24), which is derived from the Eq. (19)–(22).

$$\frac{V^B - V^A}{\Delta t} = V^n \nabla \cdot [(\mathbf{u} \cdot \mathbf{A})^B - (\mathbf{u} \cdot \mathbf{A})^n] \tag{19}$$

$$\frac{(\rho V)^B - (\rho V)^A}{\Delta t} = 0 \tag{20}$$

$$\frac{(\rho V \mathbf{u})^B - (\rho V \mathbf{u})^A}{\Delta t} = -V^n [\nabla (p^B - p^n)] \tag{21}$$

$$\frac{(\rho V I)^B - (\rho V I)^A}{\Delta t} = -V^n p^n \nabla \cdot [(\mathbf{u} \cdot \mathbf{A})^B - (\mathbf{u} \cdot \mathbf{A})^n] \tag{22}$$

$$p^B = \rho^B \frac{R}{M} T^B \tag{23}$$

Defining $\delta p = p^n - p^B$, the elliptic pressure equation can be derived as

$$\Delta t^2 \nabla \cdot \left[\frac{\mathbf{A} V^n \nabla \delta p}{(\rho V)^A \left(1 + \frac{\Delta t \mathbf{c_d} \mid \mathbf{u}^n \mid}{2\Delta x}\right)} \right] - \frac{V^A}{V^n(p^A + C)} \delta p$$
$$= \frac{V^A(p^n - p^A)}{V^n(p^A + C)} + \Delta t \nabla \cdot [((\mathbf{u} \cdot \mathbf{A})^A - (\mathbf{u} \cdot \mathbf{A})^n)] \tag{24}$$

where the coefficient, for an ideal gas, is $C = p^n \left(\frac{R}{M \cdot c_v(T)}\right)^A$.

At the third phase, an explicit convection remapping operation is implemented. At this step, the Lagrangian nodes are remapped to the Euler mesh. In GASFLOW-MPI, the Euler mesh, the computational mesh size, is fixed and never changes in time. Therefore, the Euler mesh size at t^n (V^n) is equal to the Euler mesh size at t^{n+1} (V^{n+1}), as shown in Eq. (25).

$$V^{n+1} = V^n \tag{25}$$

$$\frac{(\rho V)^{n+1} - (\rho V)^B}{\Delta t} = -\sum_f (\rho \mathbf{A} \cdot \mathbf{u})^B_f \Delta S_f \tag{26}$$

$$\frac{(\rho V \mathbf{u})^{n+1} - (\rho V \mathbf{u})^B}{\Delta t} = -\sum_f (\rho \mathbf{A} \cdot \mathbf{u} \cdot \mathbf{u})^B_f \Delta S_f \tag{27}$$

$$\frac{(\rho V I)^{n+1} - (\rho V I)^B}{\Delta t} = -\sum_f (\rho \mathbf{A} \cdot \mathbf{u} I)^B_f \Delta S_f \tag{28}$$

$$p^{n+1} = \rho^{n+1} \frac{R}{M} T^{n+1}. \tag{29}$$

3.2. Van Leer MUSCL algorithm

It has been demonstrated that the first-order accuracy scheme introduced too large numerical viscosity. Hence, a well-known second-order accuracy scheme, van Leer MUSCL scheme, is performed for convection term in order to resolve the turbulent structure. After the integration over the control volumes, the convection terms of species mass, momenta, and energy in Equations (26) through (28) could be expressed as:

$$\sum_f (\phi A u)^B_f \Delta S_f = \begin{cases} \langle \phi A u \rangle^B_E \delta y \delta z - \langle \phi A u \rangle^B_W \delta y \delta z + \\ \langle \phi A v \rangle^B_N \delta x \delta z - \langle \phi A v \rangle^B_S \delta x \delta z + \\ \langle \phi A w \rangle^B_T \delta x \delta y - \langle \phi A w \rangle^B_B \delta x \delta y \end{cases} \tag{30}$$

Table 1
Jet flows classification.

	Ma	Re	Shock wave	Classification
Subsonic	0.16	0.95×10^5	No	Incompressible
Transonic	0.90	6.6×10^5	No	Compressible without shock wave
Perfectly-expanded Supersonic	1.40	1.2×10^6	No	
Under-expanded Supersonic	3.20	7.5×10^6	Yes	Compressible with shock wave

where the transport physical quantity ϕ is ρ, $\rho\mathbf{u}$, and ρI, respectively. Taking the East (E) surface of computation cell (I, J, K) for example, the transport physical quantity ϕ on this surface could be calculated as following:

$$\langle \phi A u \rangle_{i+\frac{1}{2}}^B = \begin{cases} A_{i+\frac{1}{2}} u_{i+\frac{1}{2}}^B \{\phi_i^B + \frac{1}{2}[\delta x_i - u_{i+\frac{1}{2}}^B \delta t]S_i\}; & u_{i+\frac{1}{2}}^B \geqslant 0 \\ A_{i+\frac{1}{2}} u_{i+\frac{1}{2}}^B \{\phi_{i+1}^B + \frac{1}{2}[\delta x_{i+1} + u_{i+\frac{1}{2}}^B \delta t]S_{i+1}\}; & u_{i+\frac{1}{2}}^B \leqslant 0 \end{cases}$$

$$\text{where} \begin{cases} S_i = \frac{\phi_{i+1}^B - \phi_{i-1}^B}{\delta x_{i+\frac{1}{2}} + \delta x_{i-\frac{1}{2}}}; & u_{i+\frac{1}{2}}^B \geqslant 0 \\ S_{i+1} = \frac{\phi_{i+2}^B - \phi_i^B}{\delta x_{i+\frac{3}{2}} + \delta x_{i+\frac{1}{2}}}; & u_{i+\frac{1}{2}}^B \leqslant 0 \end{cases} \tag{31}$$

In order to track the shock wave, the original blend flux method is employed in the pressure-based all-speed flow algorithms. The basic idea is to blend of first-order scheme and second-order scheme to resolve the suddenly changed profiles near the shock, as shown in Eq. (32), where α is the blending coefficient. The main shortcoming of this method is that the user-define parameter α is problem depended and several calculation attempts are always required (Karki and Patankar, 1989, Demirdžić, et al., 1993).

$$\begin{cases} S_i = \frac{\phi_{i+1}^B - \phi_{i-1}^B}{\delta x_{i+\frac{1}{2}} + \delta x_{i-\frac{1}{2}}} \cdot \alpha; & u_{i+\frac{1}{2}}^B \geqslant 0 \\ S_{i+1} = \frac{\phi_{i+2}^B - \phi_i^B}{\delta x_{i+\frac{3}{2}} + \delta x_{i+\frac{1}{2}}} \cdot \alpha; & u_{i+\frac{1}{2}}^B \leqslant 0 \end{cases} \tag{32}$$

Different from the traditional blend numerical schemes, an advanced TVD numerical scheme is implemented in GASFLOW-MPI to capture the shock wave, as shown in Eq. (33) and (34). The main advantage of the TVD scheme is that it can adaptively switch between first-order scheme and second-order scheme according to the local velocity distribution. And no user-defined parameter is needed in the TVD scheme.

$$(S_i)_{monotone}$$
$$= \begin{cases} sign(\phi_{i+1}^B - \phi_{i-1}^B) \cdot min\left(\left(\frac{\phi_i^B - \phi_{i-1}^B}{\delta x_{i-\frac{1}{2}}}\right), \left(\frac{\phi_{i+1}^B - \phi_{i-1}^B}{\delta x_{i+\frac{1}{2}} + \delta x_{i-\frac{1}{2}}}\right), \left(\frac{\phi_{i+1}^B - \phi_i^B}{\delta x_{i+\frac{1}{2}}}\right)\right); \\ if: sign(\phi_i^B - \phi_{i-1}^B) = sign(\phi_{i+1}^B - \phi_{i-1}^B) = sign(\phi_{i+1}^B - \phi_i^B) \\ 0; \ otherwise \end{cases} \tag{33}$$

$$(S_{i+1})_{monotone}$$
$$= \begin{cases} sign(\phi_{i+2}^B - \phi_i^B) \cdot min\left(\left(\frac{\phi_{i+1}^B - \phi_i^B}{\delta x_{i+\frac{1}{2}}}\right), \left(\frac{\phi_{i+2}^B - \phi_i^B}{\delta x_{i+\frac{3}{2}} + \delta x_{i+\frac{1}{2}}}\right), \left(\frac{\phi_{i+2}^B - \phi_{i+1}^B}{\delta x_{i+\frac{3}{2}}}\right)\right); \\ if: sign(\phi_{i+1}^B - \phi_i^B) = sign(\phi_{i+2}^B - \phi_i^B) = sign(\phi_{i+2}^B - \phi_{i+1}^B) \\ 0; \ otherwise \end{cases} \tag{34}$$

4. Numerical results

For the practical safety analysis in NPPs containment, due to complex geometric conditions around the break, there is a wide spectrum of gas flow in the containment, such as free turbulent jets, impinging jets and plumes (Carasik et al., 2017). However, turbulent jet flow, as a fundamental physical phenomenon, has been experimented on different Mach number, allowing comparisons with the numerical results. In this section, four cases of the round turbulent jet flow covering subsonic, transonic and supersonic are selected to validate the all-speed turbulent flow capability in GASFLOW-MPI. In our study, the GASFLOW-MPI version 1.1 is used.

4.1. Problem description

Firstly, the main transportation of gas mixture in the NPPs containment is incompressible turbulent flow as mentioned above, therefore a subsonic turbulent jet (Hussein et al., 1994) is implemented. As for the compressible effect, a transonic jet (Stromberg et al., 1980) is calculated in this study. Besides, two simulation cases are performed for the high Mach number flow to fully validate the capability of GASFLOW-MPI. One is perfectly-expanded supersonic case (without shock wave) and the other is an under-expanded supersonic case (with shockwave). For the former one (Panda and Seasholtz, 1999), the nozzle pressure is just equal to the environmental pressure, therefore, there is no shock wave structure in the near field, while the whole flow field distribution is measured in the experiment. Because shock wave is a key feature of detonation, a strong pressure wave will cause severe damage to the containment structure. An under-expanded supersonic case (Ladenburg et al., 1949) is analyzed complementally to validate the shock wave capture capability. In this case, the shock wave experimental data in the near field is provided but without data of the far turbulent field. The classification of these four turbulent jet cases is summarized in Table 1, based on whether the jet flow is compressible and whether the shock wave is formed. It should be noted that the transonic and perfectly-expanded supersonic are divided into the same class featured with compressible flow but without shock wave, as shown in Table 1.

The round turbulent jet simulations are implemented on a cylindrical domain, as shown in Fig. 2. The size of the computational domain is summarized in Table 2. The same computational domain with the length of 23.75D and radius of 5.5D (D is the diameter of the inlet jet) is employed for the subsonic, transonic and perfectly-expanded supersonic jet flow. The computational domain is divided into uniform grids in the streamwise and azimuthal directions and non-uniform grids in the radial direction which is refined to resolve the turbulent structure in the free shear layer. The distribution of the radial direction mesh size is shown in Fig. 3, with the minimum mesh size of 0.015D near the free shear layer, and the maximum value at the outer surface of 0.045D. A smaller computational domain with the length of 4.0D and radius of 3.0D is employed for the under-expanded supersonic jet, because we only focus on the near field. A fine grid in the streamwise and radial direction near the nozzle is employed to resolve the shock wave, as shown in Table 2. The computational domain is divided into 235 × 166 × 96 nodes in the axial, radial, and azimuthal direction respectively.

All the jet turbulent cases employ the same boundary conditions as summarized in Table. 3. The Mach number of the four cases in this study varies over a large range from 0.16 (subsonic) to 3.2 (supersonic). The inlet boundary is set as the fixed velocity boundary condition with velocity profile in the radial direction as shown in Eq. (35), according to the suggestion from reference Gohil et al. (2014). The boundary condition at the x = 0 outside the nozzle is set as a free slip wall boundary condition for the low Mach number jet flow, while a small freestream ($0.02 \times U_{inlet}$) boundary condition for compressible jet flow to maintain well-posed boundary conditions as suggested in reference (DeBonis and Scott, 2002). Zero-gradient boundary, also called continuous boundary condition, is posed at the other boundaries, as shown in Fig. 2. It should be noted that for the compressible cases an additional buffer zone is used at the free outlet and at the free radial boundaries to avoid the
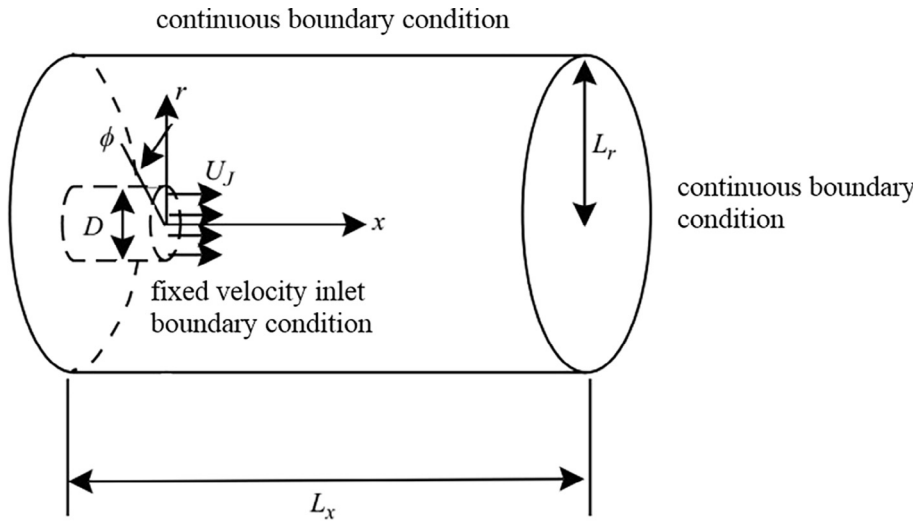
Fig. 2. Turbulent jet flow configuration.

Table 2
Computational domain and mesh size.

	Subsonic	Transonic	Perfectly-expanded Supersonic	Under-expanded Supersonic
Grid size	5.68×10^6	5.68×10^6	5.68×10^6	3.75×10^6
L_r	$5.5D$	$5.5D$	$5.5D$	$3.0D$
L_x	$23.75D$	$23.75D$	$23.75D$	$4.0D$
$\Delta r_{min}/D$	0.015	0.015	0.015	0.0125
$\Delta x_{min}/D$	0.075	0.075	0.075	0.0125
N_θ	96	96	96	96
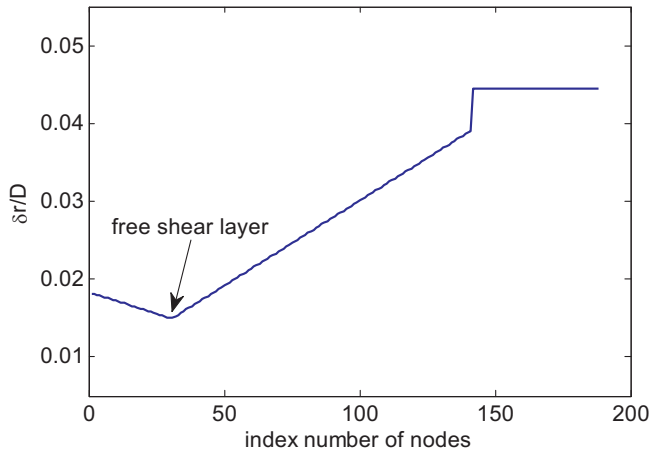
Fig. 3. Radial mesh size distribution.

Table 3
Inlet boundary parameters.

	Temperature	Velocity	Pressure	Patm
Subsonic case	300 K	56.2 m/s	1.01 MPa	1.01 MPa
Transonic case	275 K	316 m/s	1.07 MPa	1.07 MPa
Perfectly-expanded Supersonic case	216 K	411 m/s	0.98 MPa	0.98 MPa
Under-expanded Supersonic case	247 K	315.6 m/s	2.72 MPa	1.01 MPa

acoustic wave reflection, where large mesh size is used to dissipate the acoustic waves. And the zero-gradient boundary condition is defined at the outside of buffer zone.

The time step in the current simulations is self-adjusted to limit the CFL number below 0.25. The maximum CFL is set to 0.25 to capture the fluctuation information even though larger CFL numbers can be used.

$$u_i^{profile}(r) = \frac{U_{inlet}}{2}\left\{1 + \tanh\left[\frac{D/2-r}{2\theta_m}\right]\right\}$$

(35)

where θ_m is the momentum thickness of the shear layer at the nozzle exit, and $D/\theta_m = 40$.

4.2. Results and discussion

According to the classification of the turbulent jet flow, as shown in Table 1, the results of a spatially developing turbulent jet are discussed in three subsections. Firstly, the subsonic jet flow results are presented using both instantaneous flow field and mean flow field. Then the results of compressible without shock wave turbulent jet flow, including transonic and perfectly-expanded supersonic jet, are presented. The comparisons between transonic and perfectly-expanded supersonic jet are made to discuss the effect of compressibility on centerline velocity decay rates. Finally, the shock wave structure of under-expanded supersonic jet is analyzed.

The standard Smagorinsky model is employed to model the turbulent behavior at the sub-grid scale within the filtered NS equations. With the help of instantaneous flow data, the mean flow field, turbulent information and shock wave structure are analyzed. It should be noted that the averaged physical quantities are obtained by averaging instantaneous quantities in time and along the azimuth direction.

4.2.1. Subsonic jet

A subsonic turbulent jet is performed and the simulation results are presented and discussed in this subsection since that the main transportation of gas mixture is in the domain of incompressible flow. The instantaneous velocity distribution in an r-x plane is presented in Fig. 4.
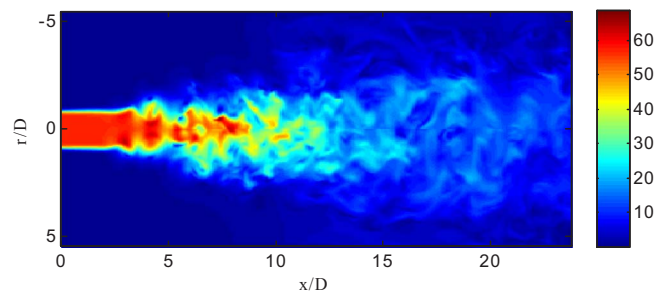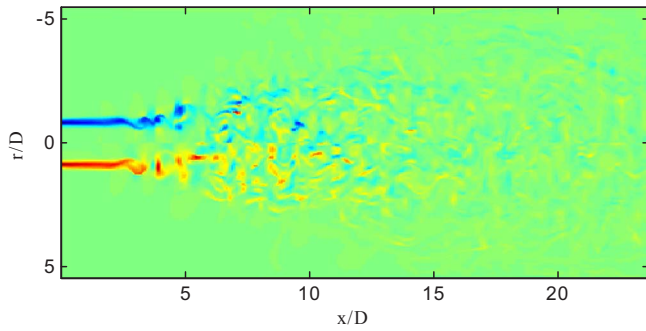

Fig. 4. Instantaneous velocity distribution in r-x plane.

Fig. 5. Instantaneous vorticity distribution in r-x plane.

Apparently, the turbulent jet flow could be divided into several regions according to its flow state Gohil et al. (2014), i.e. potential core region, transition region and fully developed region. Firstly, the potential core region near the inlet is a steady axisymmetric laminar flow. There is an axisymmetric shear layer between the entering fluid and ambient fluid, which causes a Kelvin–Helmholtz instability generating a rollup into the vortical structures at about $x = 3D$, as shown in Fig. 5. These primary vortical structures in the mixing layer come into azimuthally unstable and generate a sequence of secondary instability which is illustrated in the intermediate-field of the jet. As a consequence, the potential core reaches its end point at approximately $x = 5D$ with the instability development, meanwhile, the flow enters the transition region where flow state begins to transform from the laminar state to the turbulent state under the interaction among flow structures. The jet begins to spread radially in this region with the velocity along the centerline beginning to decay, and the shear layer beginning to decrease. Then the flow reaches the fully developed region where the turbulence is fully developed with the nonlinear turbulent interaction generating both small and large scales in space and time. Thus, more complex eddy structure is observed in the fully developed region, as shown in Fig. 4. The instantaneous velocity profile in a certain *r-azimuth* plane shows significant asymmetry in the azimuth direction due to the random turbulent fluctuations, as shown in Fig. 6, while the time-averaged velocity distribution in the azimuth direction should be symmetrical according to the symmetry of physical conditions.

The profile of the normalized streamwise velocity are comparable for the experimental data sets (Reynolds numbers of 103,000 (Crow and Champagne, 1971), 32,000 and 64,000 (Zaman and Hussain, 1980) with the LES results (Re = 0.95×10^5), as shown in Fig. 7. The flow
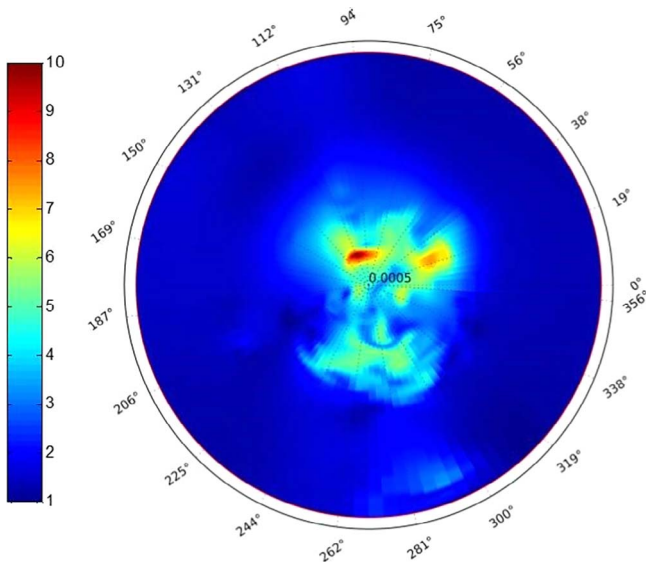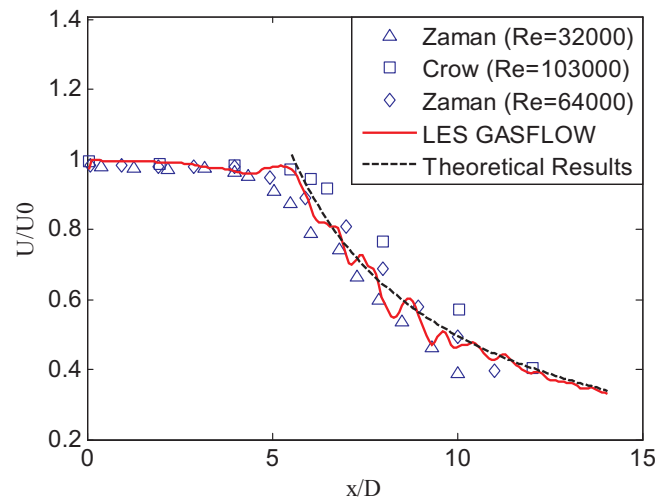

Fig. 7. Time-averaged streamwise velocity in centerline (subsonic case).

state is the laminar state in the potential core region with the streamwise velocity maintaining as constant. While the streamwise velocity begins to decay under the effect of instability in the transition region where the flow field begins to transfer from laminar into turbulence. The simulated result of the potential core length in this case is about 5D which agrees well with the experimental range of $4 < x/D < 5.5$ (Crow and Champagne, 1971). The decay rate of streamwise velocity in the turbulent region can be expressed with the Eq. (36).

$$\frac{U_{inlet}}{u(x,r=0)} = \frac{1}{B_u}\left[\frac{x}{D} - \frac{x_0}{D}\right] \qquad (36)$$

where B_u is the decay rate of the round jets. For this subsonic case, the decay rate B_u equals to 4.362, as shown in Fig. 7. In general, the simulated centerline velocity profile is in good correspondence with the experiments.

The time-averaged velocity profiles in the r direction are also presented and compared the experimental data from Hussein et al. (Hussein et al., 1994). The normalized time-averaged velocity profile $u(r)/U_0$ in the fully developed region could be expressed as a Gaussian function based on the non-dimensional radial coordinate $\eta = r/(x-x_0)$, as shown in Eq. (37). The profiles at several downstream locations $x/D = 17.0, 18.5, 20.0$ are compared with the experimental self-similar data available in the literature (Hussein et al., 1994), as shown in Fig. 8. The results show that the simulated velocity profiles at different downstream locations reach the self-similar state and agree quite well
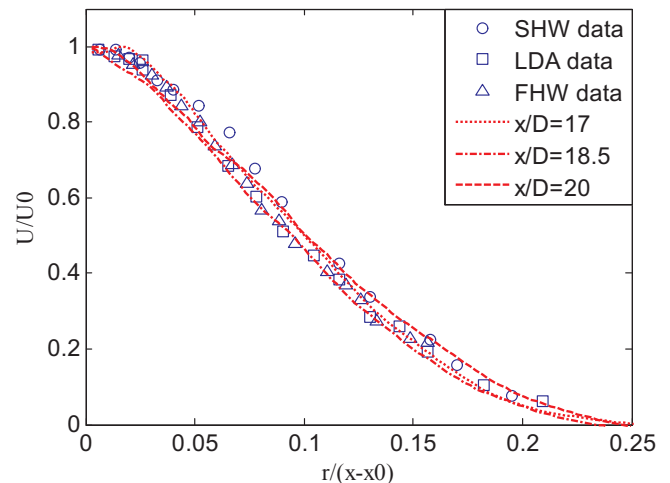

Fig. 6. Instantaneous velocity distribution in r-azimuth plane.

Fig. 8. Radial variation of the time-averaged streamwise velocity profiles.

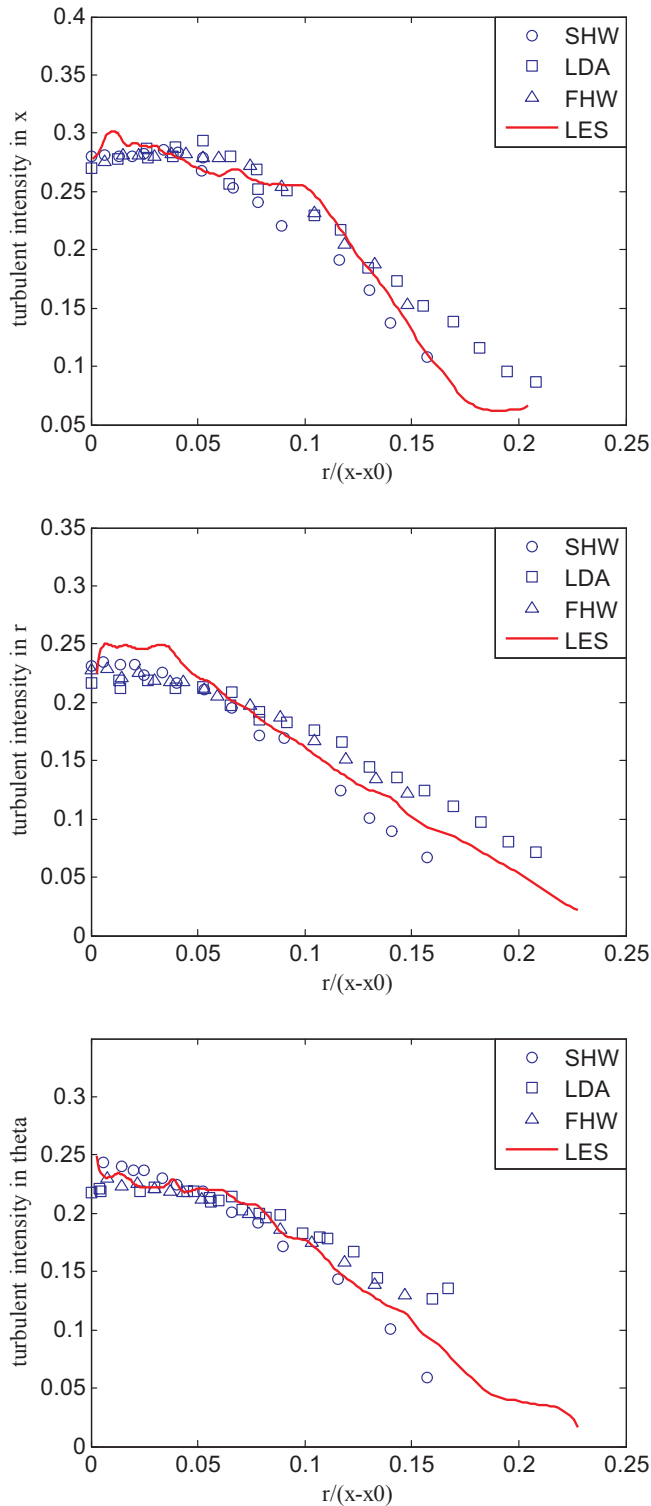**Fig. 10.** Frequency spectrum of velocity fluctuations.

Fig. 9. Radial variation of the Reynolds stress components (top) streamwise, (middle) radial, and (bottom) azimuthal.

with the experimental data sets.

$$u(r)/U_0 = \exp(-K_u\eta^2) \tag{37}$$

For a better understanding of the evolution of turbulent jet flow, the turbulent intensities in three directions ($\overline{u'^2}$, $\overline{v'^2}$ and $\overline{w'^2}$) are computed by LES, as shown in Fig. 9. All the turbulent intensities reach the maximum value near the centerline, and then decreases gradually with the increase of distance from the centerline. The computational results
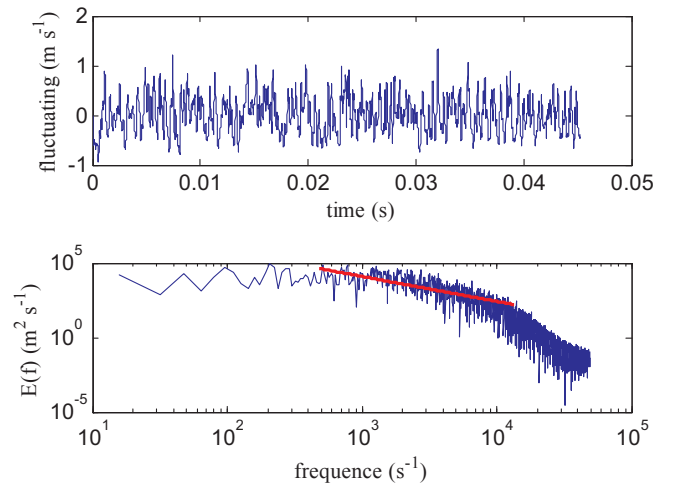
are also compared with the experimental data (Hussein et al., 1994), where the turbulent intensities are nondimensionalized using the square of the local centerline velocity U_0. The computational turbulence intensity predicts well with the experimental data.

The turbulent frequency spectrum is an important parameter to analyze the turbulent structure. In this subsection, the turbulent frequency spectrum is analyzed based on the velocity fluctuations history. The sign of the streamwise velocity fluctuations during a period of 0.045 s is plotted in Fig. 10(a). The distribution of the velocity fluctuations is random, which cannot be resolved in RANS. The frequency spectrum is calculated, as shown in Fig. 10(b). In the corresponding energy spectrum, we observe a $-5/3$ energy decay for a wide range of frequencies (red line), followed by a steeper decay for $f > 10^4$. The frequency spectrum indicates that most turbulent energy is contained in lower frequencies and most turbulent dissipation occurs in high frequencies, satisfying the turbulent energy cascade decay theory.

4.2.2. Transonic jet and perfectly-expanded supersonic jet

Transonic jet and perfectly-expanded supersonic jet are analyzed in this section, since that the compressible effect is an important issue for gas mixture critical flow in containment thermal-hydraulics analysis. Both the centerline velocity distribution and the effect of compressibility on the centerline velocity profile are presented and discussed. Similar with the subsonic case, there are three different regions in the computational domain, the potential core region where the streamwise velocity is almost a constant, the transition region where the streamwise velocity begins to decay and transforms into turbulent flow, and the fully developed region where the turbulence is fully developed. The centerline Mach number distribution of transonic flow case ($Ma = 0.9$) is shown in Fig. 11, and compared with the theoretical expectation as well as the experimental data reported by Stromberg et al. (1980). The good agreement has been reached with the decay rate B_u of 7.5804, as shown in Fig. 11. The velocity profile along centerline for the supersonic case ($Ma = 1.4$) with the decay rate B_u of 9.6455 is presented and compared with the experimental data in the literature (Panda and Seasholtz, 1999) in Fig. 12. The LES simulation result of the high Mach number case is also in good agreement with the experimental data sets.

The decay rate B_u varies with Mach numbers in the last two cases, i.e. the decay rate increases from 7.5804 to 9.6455 when the speed of jet flow increases from transonic to supersonic. Therefore, the effect of flow compressibility on centerline velocity decay rates is further discussed here. Numerical results indicate that the decay rate increases with the Mach number. This phenomenon is confirmed by the experiments of Birch and Eggers (1972), Bogdanoff (1983) and Papamoschou and Roshko (1988). They observed that the compressibility has a significant effect on growth rate of free shear flow by influencing the
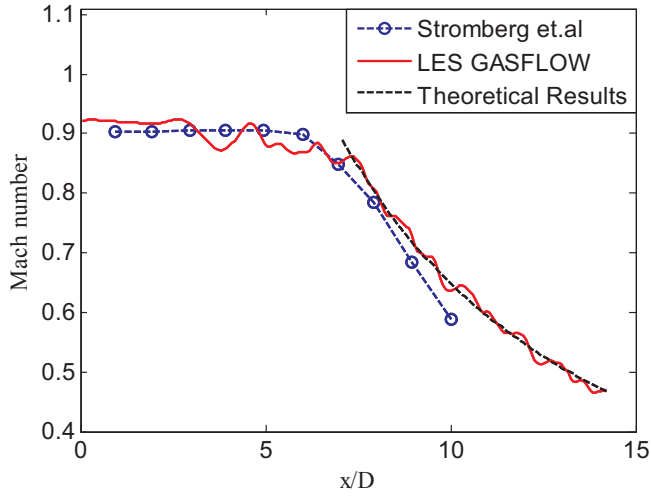
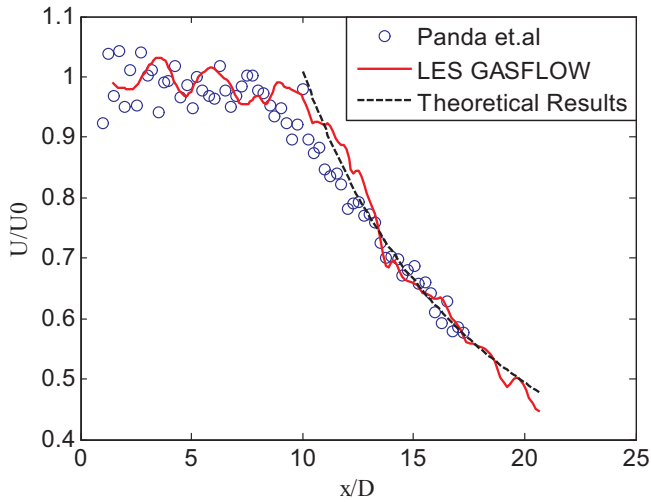**Fig. 11.** Time-averaged Mach number in centerline (transonic case).

Fig. 12. Time-averaged streamwise velocity in centerline (supersonic case).

Kelvin–Helmholtz instability growth rates and the length of the potential core. The growing shear layer is a significant source to break up the potential core and transform the jet into a fully turbulent self-similar flow. The growth rate of the free shear layer reduces with the increasing of Mach number. Then, the potential core and transition region are extended and the fully turbulent region is delayed, hence the decay rate increases. As a result, the compressibility of inlet flow influences the decay rate B_u. The compressibility effect observed from the LES simulation is consistent with the experimental data and the flow instability theory.

To further validate the LES numerical results, the time-averaged velocity profiles along the radial direction are presented and compared with the experimental data. The radial profiles of time-averaged velocity at three different positions of the transonic case are shown in Fig. 13. The simulation results agree well with the experimental data. The velocity profile near the inlet is dominated by the inlet conditions, as shown in Fig. 13 ($x = 1D$), indicating the centerline velocity in the core region remains constant and equals to the inlet velocity. And then, the velocity begins to spread radially because of the free shear layer between the entering fluid and the quiescent medium, as shown in Fig. 13 ($x = 5D$). There is a small discrepancy between simulation results and experimental data beyond $r = 0.5D$. A similar phenomenon was observed in the DNS simulation of this transonic jet experiment (Freund, 2001)). One possible reason is that this discrepancy may be
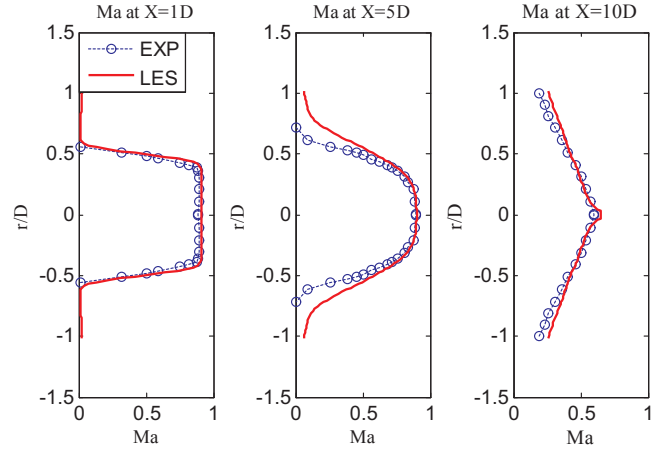
caused by measurement uncertainty. The velocity profile satisfies Gaussian distribution when the jet flow finally enters the fully developed regions under the influence of turbulence, as shown in Fig. 13 ($x = 10D$). The time-averaged velocity profiles of the perfectly-expanded supersonic case are presented and compared with experimental data of corresponding measuring points respectively, as shown in Fig. 14. The simulation results show similar tendency with the transonic case, and also agree well with the experimental data.

4.2.3. Under-Expanded supersonic jet

The shock wave behavior is one of the key features in detonation. However, the shock wave prediction is one of the key challenges in supersonic or transonic flow calculation due to its discontinuous change in pressure, temperature and density near the shock wave. Therefore, an under-expanded supersonic jet with a complex shock structure near the inlet is performed in this subsection. Here we focus on the near-field flow prediction, especially the shock wave capture. The validation of the shock wave capture capability could provide a cornerstone for the LES-based detonation model development for GASFLOW-MPI.

A round under-expanded supersonic jet flow could be divided into several regions with the Mach number distribution (Wilkes et al., 2006). Hence, a schematic diagram is employed to present the typical patterns of a jet for convenient description, as shown in Fig. 15. The Mach number at a nozzle equals to 1 with a pressure greater than the environmental pressure in region (1), as shown in Fig. 15. Then the fluid undergoes a Prandtl-Meyer expansion where the flow rapidly accelerates to higher Mach numbers and the pressure and density decreases in the regions (2) and (3). A continuous series of expansion
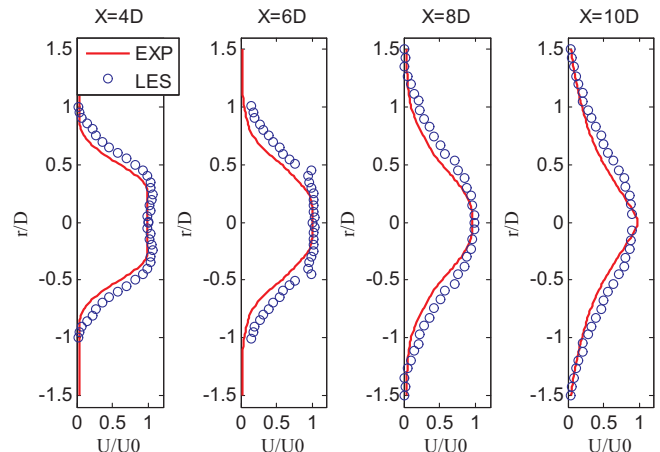

Fig. 13. Time-averaged radial profiles of streamwise velocity (transonic case).
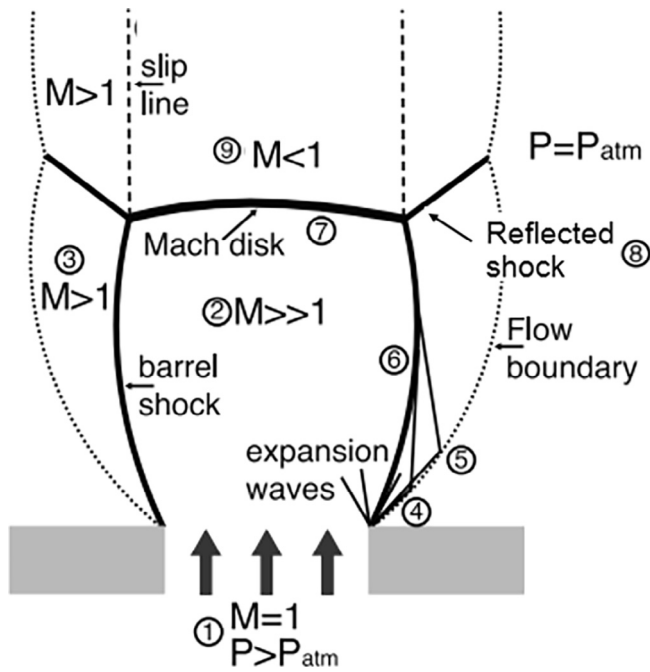

Fig. 14. Time-averaged radial profiles of streamwise velocity (supersonic case).

Fig. 15. Flow structure of a round under-expanded supersonic jet.

Fig. 17. Comparison of Mach number profiles along axis of supersonic jet.

wave form at the nozzle orifice (4), and then the pressure of the ambient gas at the boundary pushes the over expanded fluid back as compression waves (5). These compression waves coalesce to form a complex shock structure, including barrel shock (6), Mach disk (7) and reflected shock (8). The barrel shock, reflected shock, and Mach disk meet at a point which is named as shock triple point.

The density distribution of the under-expanded supersonic jet is presented and compared with the experimental data from the literation (Ladenburg et al., 1949), as shown in the Fig. 16. The density distribution in this Prandtl-Meyer expansion region is compared with the experiment. The contour distribution of density agrees well with the experimental data sets, as shown in Fig. 16. All these three types of
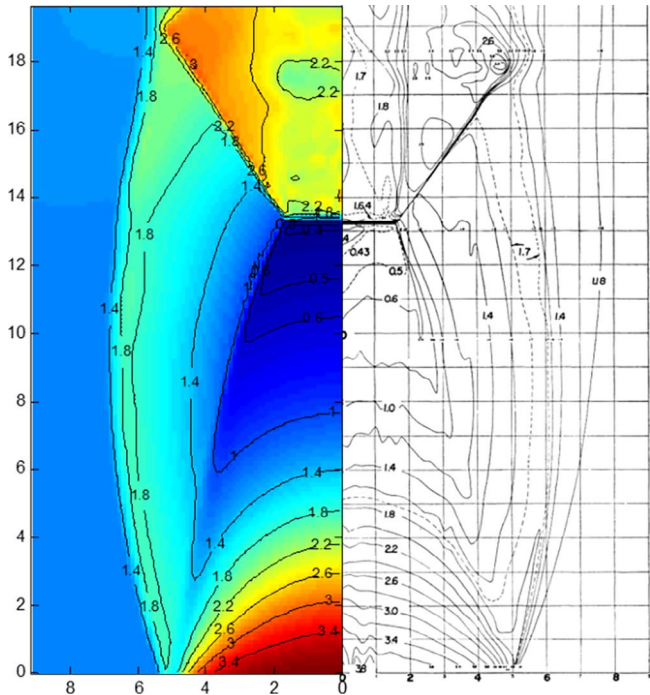
shock, including barrel shock, Mach disk and reflected shock, are captured by the second-order accuracy TVD scheme in GASFLOW-MPI and no parasitic oscillation occurs near the shock, as shown in Fig. 16. Furthermore, the location is shock wave triple point is compared with the Ladenburg experiment. The experimental data is obtained by analysis of an interferogram, as shown in Fig. 16, indicating the triple point at (13.3, 1.7) mm. Our simulation manages to capture this phenomenon with location error < 3% of the experimental data in the x direction. The location error of 0.38 mm in the x direction seems to be caused by inlet conditions difference between the experiment and simulation. Meanwhile, the Mach number profile at the centerline is also presented and compared with the experiment. The Mach number grows up to 3.2 in the Prandtl-Meyer expansion region, and then decreases to the subsonic flow rapidly when passing through the Mach disk, as shown in Fig. 17. The Mach number profile is in good correspondence with the experiments. To summarize above, the second-order accuracy TVD scheme, Van Leer MUSCL Algorithm, is accurate enough to capture the complex shock structure for multi-dimension problem.

5. Conclusion

According to the report of Containment Code Validation Matrix, the all-speed turbulent flow capability is required to simulate the turbulent flow at a broad range of Mach numbers in the NPPs containment due to the broad variety of accident scenarios. In this paper, the simulations of four turbulent jet cases from subsonic to supersonic are performed to validate the GASFLOW-MPI code. The large eddy simulation (LES) turbulent model is employed to capture detailed turbulent information of the flow. With the help of the instantaneous and time-averaged flow distribution and turbulent statistics, the flow field is analyzed and compared with the experimental data. The results show that the simulation results are in good agreement with the experimental data. In detail, conclusions can be drawn as below:

1) For the subsonic case, the numerical results show that the velocity distributions, including the centerline velocity and the streamwise velocity, agree well with the experimental data. What's more, the turbulence intensity in the fully developed region also predicts well with the experimental data, revealing the -5/3 law velocity power spectrum. The simulation results further validate the capability of GASFLOW-MPI to predict the incompressible turbulent flow in NPP containments.

2) For the compressible flow without shock involved, including transonic and perfectly-expanded supersonic jets, the size of the potential core and the velocity distribution agree well with the

Fig. 16. Density distribution in r-x plane.

experimental data. Furthermore, the compressibility effect on a free shear flow is discussed, and its result is consistent well with the previous experimental data. These results demonstrate that the compressible effect could be predicted reasonably in GASFLOW-MPI.

3) For the compressible jet flow involving shock waves, there is a complex shock wave structure near the inlet, including a barrel shock, a reflected shock, and a Mach disk. The result indicates that all these three types of shock are accurately captured by the Van Leer MUSCL scheme in GASFLOW-MPI and no parasitic oscillation occurs near the shock which provides a basis to capture the chemically-driven shock waves in the NPPs.

In conclusion, the turbulent jet flow at a broad range of Mach numbers, including subsonic, transonic and supersonic flow, can be successfully simulated using the unified numerical solution algorithm in one single scientific computing software GASFLOW-MPI. The good agreement to the experimental data confirms the powerful feature of GASFLOW-MPI in the simulation of turbulent flow at all-speed. Further investigations and developments will be performed to allow large eddy simulations of turbulent flow in full-scale NPP containments using GASFLOW-MPI. More advanced numerical scheme development, such as WENO scheme, is also in the plan to capture the shock cell/turbulent interaction.

References

Balzek, J., 2001. Computational Fluid Dynamics: Principles and Applications. Elsevier Science, Oxford.

Benz, S., Royl, P. Band, S., 2013. Analysis of a hypothetical loss of coolant accident in a Konvoi type NPP by GASFLOW and COCOSYS. In: Proceedings of Jahrestagung Kerntechnik, Berlin.

Birch, S.F., Eggers, J.M., 1972. A Critical Review of the Experimental Data on Turbulent Shear Layers, NASA SP 321.

Bogdanoff, D.W., 1983. Compressibility effects in turbulent shear layers. AIAA J. 21 (1983), 926–927.

Breitung, W., 1999. SOAR on Containment Thermal Hydraulics and Hydrogen Distribution, NEA/CSNI/2000/7. OECD, Paris, France.

Carasik, L.B., Sebilleau, F., Walker, S.P., Hassan, Y.A., 2017. Numerical simulations of a mixed momentum-driven and buoyancy-driven jet in a large enclosure for nuclear reactor severe accident analysis. Nucl. Eng. Des. 312, 161–171.

Chen, G.Q., 2001. Shock capturing and related numerical methods in computational fluid dynamics. Acta Math. Univ. Comenianae Proc. Algoritmy 2001, 51–73.

Chin, Y.S., Mathew, P., Glowa, G., et al., 2014. Containment Code Validation Matrix," Organisation for Economic Co-Operation and Development, Nuclear Energy Agency-OECD/NEA, Committee on the Safety of Nuclear Installations-CSNI, Le Seine Saint-Germain, 12 boulevard des Iles, F-92130 Issyles-Moulineaux (France).

Crow, S.C., Champagne, F.H., 1971. Orderly structure in jet turbulence. J. Fluid Mech. 48 (1971), 547–591.

DeBonis, J.R., Scott, J.N., 2002. Large-eddy simulation of a turbulent compressible round jet. AIAA J. 40 (7).

Demirdžić, I., Lilek, Ž., Perić, M., 1993. A collocated finite volume method for predicting flows at all speeds. Int. J. Num. Met. Fluids 17 (1993), 1029–1050.

Dimmelmeier, H., Eyink, J., Movahed, M.A., 2012. Computational validation of the EPR™ combustible gas control system. Nucl. Eng. Des. 249, 118–124.

Ferziger, J.H., Peric, M., 1996. Computational Methods for Fluid Dynamics. Springer-Verlag, New York.

Fluent, A.N.S.Y.S., 2011. Ansys fluent theory guide. ANSYS Inc. USA 15317, 724–746.

Garnier, E., Adams, N., Sagaut, P., 2009. Large Eddy Simulation for Compressible Flows. Springer.

Grotzbach, G., Worner, M., 1999. Direct numerical and large eddy simulations in nuclear applications. Int. J. Heat Fluid Flow 20 (1999), 222–240.

Hassan, Y.A., 2008. Large eddy simulation in pebble bed gas cooled core reactors. Nucl. Eng. Des. 238 (2008), 530–537.

Heinz, S., 2003. A model for the reduction of the turbulent energy redistribution by compressibility. Phys. Fluids 5 (11), 3580–3583.

Hirt, C.W., Amsden, A.A., Cook, J.L., 1974. An arbitrary Lagrangian-Eulerian computing method for all flow speeds. J. Comput. Phys. 14 (1974), 227–253.

Hussein, H.J., Capp, S.P., George, W.K., 1994. Velocity Measurements in a High-Reynolds-Number, Momentum-Conserving, Axisymmetric, Turbulent Jet. J. Fluid Mech. 258 (1994), 31–75.

IAEA, 2011. Fukushima Daiichi Status Report, Vienna.

Freund, Jonathanb, 2001. Noise sources in a low-Reynolds-number turbulent jet at Mach 0.9. J. Fluid Mech. 438, 277–305.

Karki, K.C., Patankar, S.V., 1989. Pressure based calculation procedure for viscous flows at all speeds in arbitrary configurations. AIAA J. 27 (1989), 1167–1174.

Kaushik, M., Kumar, R., Humrutha, G., 2015. Review of computational fluid dynamics studies on jets. Am. J. Fluid Dyn. 1–11.

Kim, J., Hong, S., 2015. Analysis of hydrogen flame acceleration in APR1400 containment by coupling hydrogen distribution and combustion analysis codes. Prog. Nucl. Energy 78 (2015), 101–109.

Ladenburg, R., Van Voorhis, C.C., Winckler, J., 1949. Interferometric studies of faster than sound phenomena. Part II. Analysis of supersonic air jets. Phys. Rev. 76 (1949), 662–677.

Lee, D., 1996. Local preconditioning of the Euler and Navier-Stokes equations (PhD Thesis). University of Michigan.

Lee, W.T., 1991. Local preconditioning of the Euler equations (PhD Thesis). University of Michigan.

Li, Y., Zhang, H., Xiao, J., et al., 2018. Numerical investigation of natural convection inside the containment with recovering passive containment cooling system using GASFLOW-MPI. Ann. Nucl. Energy 114 (2018), 1–10.

Nieuwstadt, F.T.M., Mason, P.J., Moeng, C.H., Schumann, U., 1993. Large Eddy simulation of the convective boundary layer: a comparison of four computer codes. Turbulent Shear Flow 8 (1993), 343–367 Springer-V Berlin.

Panda, J., Seasholtz, R.G., 1999. Velocity and temperature measurement in supersonic free jets using spectrally resolved rayleigh scattering. AIAA Paper 99–0296.

Papamoschou, D., Roshko, A., 1988. The compressible turbulent shear layer: an experimental study. J. Fluid Mech. 197 (1988), 453–477.

Patankar, S.V., Spalding, D.B., 1972. A calculation procedure for heat, mass and momentum transfer in three-dimensional parabolic flows. Int. J. Heat Mass Trans. 15 (1972), 1787–1806.

Piomelli, U., 1999. Large eddy simulation: achievements and challenges. Prog. Aerosp. Sci. 35 (1999), 335–362.

Royl, P., Müller, C., Travis, J. R., et al., 1995. Validation of GASFLOW for analysis of steam/hydrogen transport and combustion processes in nuclear reactor containments. In: Procs 13th Conference on Structural Mechanics in Reactor Technology, Porto Alegre, RS, Brazil.

Royl, P., Travis, J.R., Kim, J., 2014. GASFLOW-III: a computational fluid dynamics code for gases, aerosols and combustion, Volume 3: Assessment Manual". Karlsruhe Inst. Technol. Rep., Rev. 1.

Royl, P., Xiao, J., Jordan, T., 2016. Blind Simulations of THAI Test TH27 with GASFLOW-MPI for Participation in the International Benchmark Conducted within the German THAI Program. In: Workshop Application of CFD/CFMD Codes September 13–15, Cambridge, Ma, USA.

Salmanzadeh, M., Rahnama, M., Ahmadi, G., 2010. Effect of sub-grid scales on large eddy simulation of particle deposition in a turbulent channel flow. Aer. Sci. Technol. 44 (9), 796–806.

Sarikurt, F.S., Hassan, Y.A., 2017. Large eddy simulations of erosion of a stratified layer by a buoyant jet. Int. J. Heat Mass Transf. 112, 354–365.

Sesterhenn, J., Müller, B., Thomann, H., 1999. On the cancellation problem in calculating compressible low mach number flows. J. Comput. Phys. 151 (1999), 597–615.

Smagorinsky, J., 1963. General circulation experiments with the primitive equations. Mon. Weather Rev. 91 (1963), 99–110.

Stromberg, J.L., McLaughlin, D.K., Troutt, T.R., 1980. Flowfield and acoustic properties of a mach number 0.9 jet at a low reynolds number. J. Sound Vib. 72 (1980), 159–176.

Gohil, Trushar B., Saha1, Arun K., Muralidhar, K., 2014. Large eddy simulation of a free circular jet. J. Fluids Eng. 136.

Van Leer, B., 1979. Towards the ultimate conservative difference scheme, V. A second order sequel to Godunov's method. J. Comput. Phys. 32 (1979), 101–136.

Wilkes, J., Glass, C., Danehy, P., Nowak, R., 2006. Fluorescence imaging of under-expanded jets and comparison with CFD. In: 44th AIAA aeerospace sciences meeting and exhibit. Reno, Nevada, USA. 9-12 January.

Xiao, J., Breitung, W., Kuznetsov, M., et al., 2017. GASFLOW-MPI: A new 3-D parallel all-speed CFD code for turbulent dispersion and combustion simulations: Part I: Models, verification and validation. Int. J. Hydrogen Energy 42 (12), 8346–8368.

Xiao, J., Travis, J.R., Royl, P., et al., 2016. Three-dimensional all-speed CFD code for safety analysis of nuclear reactor containment: Status of GASFLOW parallelization, model development, validation and application. Nucl. Eng. Des. 301, 290–310.

Xiao, J., Travis, J. R., Jordan, T., et al., 2014a. GASFLOW-III: A Computational Fluid Dynamics Code for Gases, Aerosols and Combustion, Volume 2: User's Manual, Karlsruhe Institute of Technology Report, Revision 3.5.

Xiao, J., Travis, J. R., Jordan, T., et al., 2014b. GASFLOW-III: A Computational Fluid Dynamics Code for Gases, Aerosols and Combustion, Volume 1: Theory and Computational Model, Karlsruhe Institute of Technology Report, Revision 3.5.

Zaman, K.B.M.Q., Hussain, A.K.M.F., 1980. Vortex pairing in a circular jet under controlled excitation. Part 1. General jet response. J. Fluid Mech. 101 (1980), 449–544.

Zeman, O., 1990. Dilatation dissipation: the concept and application in modeling compressible mixing layers. Phys. Fluids A 2 (2), 178–188.

Zhang, H., Li, Y., Xiao, J., Jordan, Thomas, 2017. Large eddy simulation of turbulent flow using the parallel computational fluid dynamics code GASFLOW-MPI. Nucl. Eng. Technol. 49 (6), 1310–1317.